JOURNAL OF SPACECRAFT AND ROCKETS
Vol. 48, No. 3, May–June 2011

Influence of Scaling Rules on Loss of Acoustic Energy

Daniel Morgenweck* and Thomas Sattelmayer†
Technical University of Munich, 85748 Garching, Germany
and
Felix Fassl‡ and Roland Kaess§
Astrium, GmbH, 81663 Munich, Germany

DOI: 10.2514/1.48334

The damping of acoustic oscillations in two different design concepts of rocket engine demonstrators is assessed. Both engines represent different scaling strategies for subscale demonstrators. In this context, one major question is which of the two designs are less prone to combustion instabilities. Different methods are presented to show the influence of geometry on the loss of acoustic energy. The decay coefficient is determined, which accounts for the overall loss of acoustic energy independent of the physical mechanism. The admittance at the intersection of the combustion chamber and nozzle is evaluated. The acoustic flux is calculated and divided into different kinds of contributions. In this regard, the importance of the relation between pure acoustic transport and convective transport is emphasized. It shows that the pure acoustic transport is directed into the combustion chamber. However, its fraction of acoustic energy is compensated by the convective transported acoustic energy, which is convected out of the thrust chamber. Thus, the overall acoustic energy in the system is decaying. The two designs show different damping characteristics for different modes. The photoscaled design is less stable for longitudinal modes but more stable for transverse modes. The first transverse mode in the Mach-scaled design is barely damped.

Nomenclature

c	=	speed of sound, m/s
E	=	perturbation energy, J/m^3
$\mathcal{E}$	=	overall acoustic energy contained in system, J
E_a	=	acoustic energy, J/m^3
H	=	Hilbert transform, Pa
I	=	perturbation flux, W/m^2
I_a	=	acoustic flux, W/m^2
M	=	Mach number
$\underline{n}$	=	normal vector
P	=	acoustic power, related to initial acoustic energy, 1/s
p	=	pressure, Pa
S	=	source term, W/m^2
T	=	one time period of excitation frequency, s
$\underline{u}$	=	velocity vector, m/s
ρ	=	density, kg/m^3
ω	=	dimensionless angular frequency
ω^*	=	angular frequency, 1/s
$\langle\,\rangle$	=	time average

Superscripts

$'$	=	perturbation quantity
$\bar{}$	=	mean quantity
$\hat{}$	=	complex quantity in frequency domain

Received 30 November 2009; revision received 8 November 2010; accepted for publication 11 January 2011.

*Graduate Engineer, Chair for Thermodynamics, Boltzmannstrasse 15; morgenweck@td.mw.tum.de.

†Professor, Chair for Thermodynamics, Boltzmannstrasse 15; sattelmayer@td.mw.tum.de.

‡Transportation Propulsion, Space Transportation, Business Division Launcher Propulsion; Felix.Fassl@astrium.eads.net.

§Transportation Propulsion, Space Transportation, Business Division Launcher Propulsion; Roland.Kaess@astrium.eads.net.

I. Introduction

TODAY, oscillating instabilities are still a major threat for liquid rocket engines. High-frequency oscillations can cause damage to the nozzle and combustion chamber as well as to the periphery. The increased heat exchange to the wall due to pressure oscillations can cause thermal failure; thus, it threatens the success of the mission. Since the beginning of modern rocket motor design, there has been the need to understand the mechanism of those instabilities. Crocco and Cheng [1] did a fundamental investigation in this field at a very early stage. It was found that the main criteria for stability of the combustion process in a rocket engine is the ratio between the input of acoustic energy by the combustion process and the loss of acoustic energy. Therefore, the loss of acoustic energy by the boundary layer is assumed to be small compared with the overall loss, whereas the nozzle is considered to have the highest damping ability [2]. Marble and Candel [3] derived an analytic relation for admittances of short nozzles depending only on the Mach number. There, the admittance characterizes the reflection behavior of the nozzle; thus, it describes to a certain degree the acoustic energy flux through the nozzle. In a more sophisticated seminumerical and experimental approach, Bell [4], Zinn [5], and Bell and Zinn [6] investigated nozzle admittances for three-dimensional (3-D) acoustic waves and for nozzles of a finite length. Although the admittance itself depends on the Mach number, it does not sufficiently describe the acoustic flux in the presence of steady mean flow. Cantrell and Hart [7] gave a formulation for acoustic energy in an isentropic potential flow. Similar relations were also found by Morfey [8] and Zinn [5]. They showed that there is an additional contribution to the acoustic energy transport related to the Mach number.

The following work uses several characteristic quantities to quantify the loss of acoustic energy in the rocket engine; they are admittance, decay coefficient, and acoustic flux. The procedure in the investigation is similar to the one used by Pieringer et al. [9,10]. Two different designs of a demonstrator thrust chamber are compared by means of these characteristic quantities. Both designs were derived from a concept of a new rocket engine by different scaling rules. It can be expected that both designs also show a different acoustic behavior. To support the decision of which demonstrator should be built, an acoustic analysis is carried out. In the following, the two different designs are compared with respect to their acoustic characteristics.

II. Numerical Method

For the numerical evaluation given in this report, the time domain solver PIANO-SAT is used. The solver is provided by the DLR, German Aerospace Center, Braunschweig [11], and it used in aeroacoustic applications. Because of its special schemes for wave propagation, it has reached broad acceptance in the field of air traffic noise prediction [12,13]. In the context of rocket thrust chambers, special adaptations for stability assessments are applied, such as a term for coupling heat release fluctuations and acoustic perturbations. To assess the onset of acoustic oscillations in operating rocket engines, a simple model for coupling combustion fluctuation and acoustic fluctuation was implemented [14]. Moreover, special boundary conditions are developed to allow the modeling of the injector plane and the absorbers in the combustion chamber. In the subsequent analysis, the boundary condition at the injector plane is set in a way that it prevents acoustic flux over the boundary. Thus, the only loss of acoustic energy appears through the nozzle. PIANO-SAT operates in the time domain and uses special discretization schemes optimized for wave propagation. Those are a time-explicit finite difference scheme of the fourth-order in space and time. The numerical method solves the linearized Euler equations (LEEs) or the acoustic perturbation equations [15]. Therefore, the primitive quantities for density, pressure, and velocity are split into a mean and a perturbation part. PIANO-SAT only solves the perturbation part. The mean quantities are input to the solver and originate from a computational fluid dynamics (CFD) computation.

The following investigations are based on the LEEs.

III. Thrust Chamber Geometry and Mean Quantities

Astrium, GmbH, is investigating a new thrust chamber design. For evaluating and investigating the new design, a subscale rocket engine is in development that will be operated on a test rig. Two different scaling approaches are discussed regarding the transferability of the demonstrator test campaign results to the master design. In this context, an important question is the susceptibility to the combustion instabilities of the two geometries. The results of this report are part of a predesign study to assess the influence of nozzle geometry on instability.

The first design is derived by means of geometrical scaling or photoscaling. Radial and axial lengths are scaled with the same scaling factors. The subscale thrust chamber is shorter and thinner than the master design. The scaled nozzle is extended by a cylindrical part to assure a similar degree of burning l^*. It constitutes the classical approach for designing a subscale demonstrator. The photoscaled design is depicted in Fig. 1a.

The second demonstrator thrust chamber is designed to achieve Mach number similarity between the demonstrator and the master design. The demonstrator thrust chamber is also called Mach-scaled design. The radial dimension is scaled in order to have a similar Mach number at the axis of symmetry. Thus, the flowfield and boundary layer are similar to the master design. This assures the heat load to the chamber wall can be investigated under more realistic conditions. The Mach-scaled design is depicted in Fig. 1b.

Figures 1a and 1b also show the planes used for the evaluation of the acoustic intensity in the study. In both thrust chambers, these planes reside at the same axial distance from the injector plane (faceplate). In the numerical acoustic analysis, pressure and velocity fluctuations are recorded over time at the circumference of the planes. The first plane is close to the injector plane. A second plane resides where the transition between the cylindrical part and nozzle may be assumed in the Mach-scaled design (at $x = 0.1$ m). The third plane marks the interface between the nozzle and cylindrical combustion chamber in the photoscaled thrust chamber (at $x = 0.25$ m).

Although the advantage of using the Mach-scaled demonstrator instead of the photoscaled demonstrator concerning the Mach number and heat load distribution is obvious, it is not clear how both designs behave acoustically. Therefore, in the design stage, the two designs are investigated numerically with PIANO-SAT. The outcome of the investigation helps to predict the loss of acoustic energy based on the geometry.

PIANO is based on the LEEs and thus solves only the perturbation part of the primitive quantities. This implies that the steady-state mean quantities are input to the acoustic solver PIANO-SAT. The mean flowfield is separately calculated by a CFD solver in a steady-state Euler or Reynolds-averaged Navier–Stokes (RANS) computation. The flowfield is then patched to the grid of the acoustic solver. Liquid oxygen is used as oxidizer, and hydrogen is used as fuel. To simplify matters, combustion itself is not considered. Instead, the material properties are frozen to the state after combustion and are set as a boundary condition at the inlet. Furthermore, the velocity is given by a block profile at the inlet. Figures 2a–2d show the results obtained with an Euler computation. Figures 2a and 2b show the Mach number distribution on a slice through the thrust chamber. It is evident that the nozzle is supercritical; that is, the flow reaches Mach 1 in the throat. This defines a well-suited condition at the downstream boundary of the acoustic domain. Because acoustic perturbations cannot travel faster than Mach 1, acoustic perturbations downstream from the Mach 1 isosurface cannot affect the acoustic field upstream inside the combustion chamber. Figures 2c and 2d depict the speed of sound distribution inside the thrust chamber. The maximum values of the speed of sound in the whole computational domain in the case of the photoscaled design is 1617 m/s, whereas for the Mach-scaled design, it is 1616 m/s. The speed of sound is directly linked via the Courant–Friedrichs–Lew (CFL) criteria to the time step,

$$\Delta t = \mathrm{CFL}\,\frac{\min(\Delta_{x,y,z})}{c + |\underline{u}|} \tag{1}$$

where $\min(\Delta_{x,y,z})$ is the minimum cell extension found in the whole computational domain, considering all three space dimensions. Analyzing Eq. (1) further, it becomes clear that grid resolution and time step are also coupled and cannot be chosen independently from

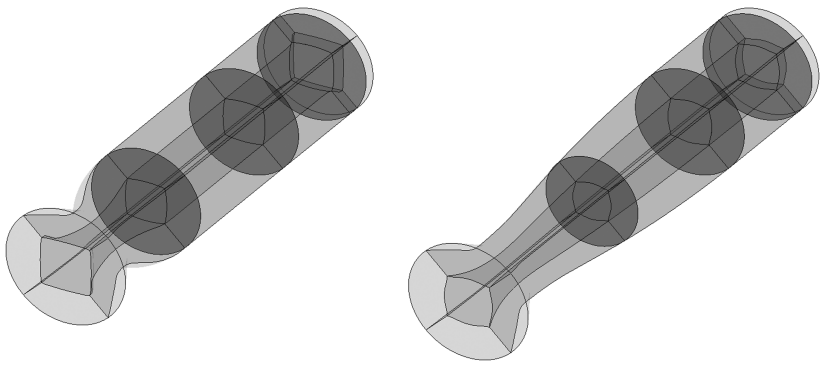

a) Photoscaled **b) Mach-scaled**

Fig. 1 Thrust chamber with planes for computation of acoustic fluxes.

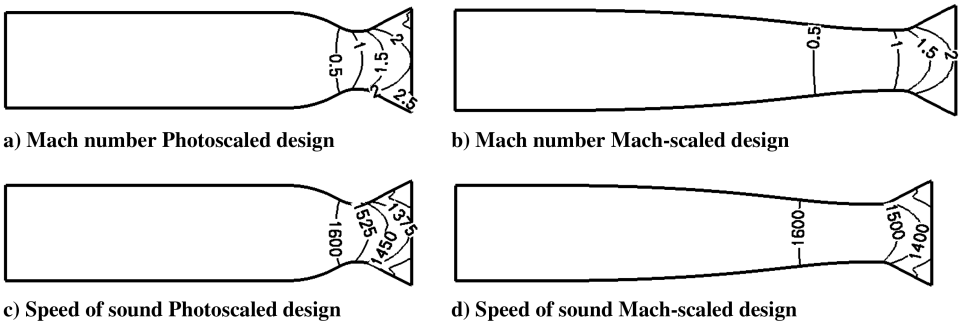

a) Mach number Photoscaled design b) Mach number Mach-scaled design

c) Speed of sound Photoscaled design d) Speed of sound Mach-scaled design

Fig. 2 Mean flowfield.

each other. Thus, improving the grid resolution means decreasing the time step, which leads to even higher computational effort. For the later analysis, the CFL number is chosen to be 0.7. The corresponding time step is $6.3e-8$ s in the case of the photoscaled design and $1.3e-7$ s for the Mach-scaled design.

Calculating the mean flowfield for the computational aeroacoustics (CAA) simulation by a CFD solver raises questions about the quality of the mean flow. The CFD solver is fairly second-order accurate, whereas the CAA approach is fourth-order accurate. To overcome this discrepancy, the grid resolution in the CFD simulation is four times higher than in the CAA calculation. Thus, it is deemed that the lack of order in the CFD is more than compensated by higher grid resolution.

IV. Validation of Method

The investigation is part of a preliminary design study on demonstrator thrust chambers. At this stage, experimental results that could be used for comparison are not available. Hence, a test campaign done in the 1970s by Bell [4] serves for validation. At that time, Zinn developed a semianalytical method to evaluate nozzle admittances [5]. Its results were validated against experiments of Bell [4] and published in [6]. A good agreement was found between the computed nozzle admittances and those obtained from the experiment. Different configurations were investigated. A set of three parameters was chosen to characterize the nozzle. The parameters were the Mach number in the cylindrical part before the nozzle, the radius R_T connecting the cylindrical part before the nozzle and the conical part of the nozzle, and the apex angle of the conical part. R_T is also the radius that characterizes the curvature leading from the subsonic part of the nozzle to the supercritical part. Typically, the curvature radius R_T is related to the radius of the cylinder R_{CY}. The conical part of the nozzle is described by the apex angle Θ. A sketch with the characteristic parameters is shown in Fig. 3.

Two different configurations were chosen to compare the capability of PIANO-SAT with data from the experiments of Bell [4]. The first configuration (Fig. 4a) has a Mach number of 0.16 at the entry of the nozzle, a ratio of radii R_T/R_{CY} of one, and an apex angle of 30 deg. The second configuration (Fig. 4b) has a Mach number of 0.08 at the entry, a ratio of radii of 0.44, and an apex angle of 15 deg. In both configurations, longitudinal modes were excited and the admittance was taken at the intersection between the cylindrical part and the nozzle. In the experiments, the impedance tube is excited by loud speakers and, in the numerical simulation, by a periodic pressure source. The results are evaluated when a limit cycle is reached. The pressure is recorded on different positions close to the nozzle. The waves are divided in downstream and upstream propagating waves; hence, the admittance is obtained. Figures 4a–4d show the results of the experiments. The real and imaginary parts of the admittance are compared with the semianalytical approach and the numerics of PIANO-SAT for the two configurations. The frequency is given in dimensionless form $\omega = \omega^* R_{\mathrm{CY}}/c_E$ normalized by the speed of sound at the entrance of the nozzle and the radius of the cylindrical part of the thrust chamber.

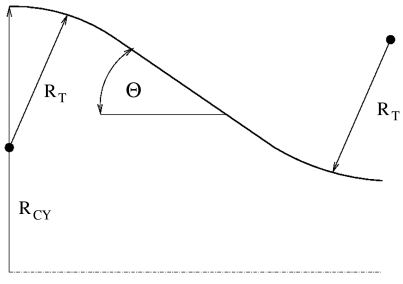

Fig. 3 Bell's nozzle parameter [4].

A good agreement between the semianalytical results (straight line) and the experiments (dots) could be discerned, but greater differences appear around the minima and maxima. This might be explained by the fact that the semianalytical approach only considers a one-dimensional flowfield. In PIANO-SAT, a full 3-D calculation is performed. It shows the numerics (triangles) meet the trend of the experiments (dots) better. Even in regions where the semianalytical approach shows deviations, the simulation of PIANO-SAT agrees well with the experiments. This leads to the conclusion that PIANO-SAT is capable of describing the acoustics in the nozzle.

V. Decay Coefficient

A criterion for stability in rocket engines is the decay coefficient. Therefore, the exponential decay of pressure fluctuations is determined. In case acoustic energy is not lost by other mechanisms than transport through the nozzle itself, the decay coefficient is a characteristic quantity for the damping of pressure oscillations by the nozzle. Unlike the admittance, it considers the convective loss of acoustic energy by mean flow.

The first step to obtain the decay coefficient is to analyze the eigenmodes in the thrust chamber: those which participate in the pressure oscillations. One way to find the dominating modes is to initially excite the oscillation in the chamber and record the decay of the pressure perturbations. This is done by setting a Gaussian pressure pulse at a certain point in the computational domain. The center of the Gaussian pulse is situated at some distance away from the axial axis to ensure that transverse modes are excited. In principle, the excitation mechanism has an influence on how strong certain modes are initiated. Therefore, the recorded pressure signal depends on the excitation. However, a Gaussian pressure pulse has the ability to excite a broad band of frequencies. Thus, the main eigenfrequencies will be excited and can be observed in the pressure signal. In Figs. 5a and 5b, the pressure records of one monitoring point opposite the Gaussian pulse are depicted for the photoscaled and Mach-scaled designs. Because the governing equations are linear, the amplitude of oscillation is proportional to the excitation amplitude. It means the level of the oscillation is a free parameter and can be adjusted arbitrarily. However, for the subsequent analysis in this report, the magnitude of the oscillations will not be considered.

Figures 5c and 5d show the eigenfrequencies obtained by means of the fast Fourier transform of the pressure signal. They are recorded at 12 equally distributed monitoring points around the first plane close to the injector head. Regarding the pressure signal from the other

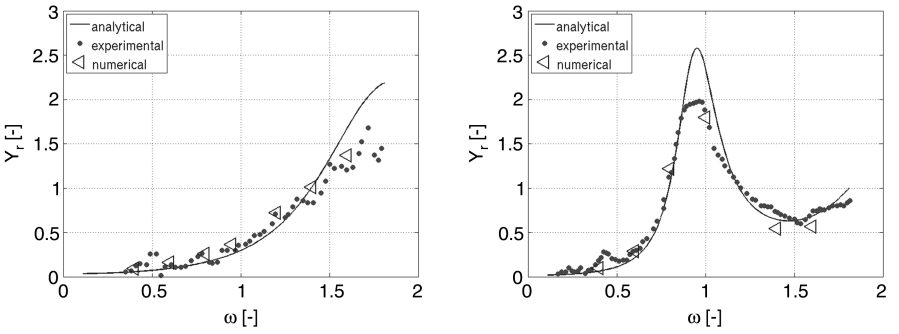

a) Real part with apex angle Θ of 30 deg, Mach number of 0.16, and radii ratio R_T/R_{CY} of 1

b) Real part with apex angle Θ of 15 deg, Mach number of 0.08, and radii ratio R_T/R_{CY} of 0.44

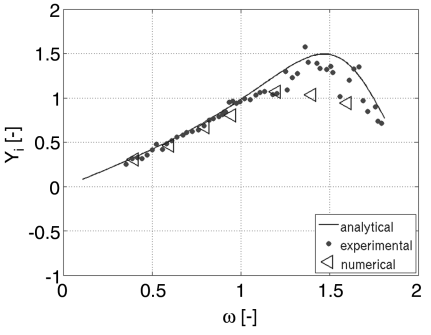

c) Imaginary part with apex angle Θ of 30 deg, Mach number of 0.16, and radii ratio of R_T/R_{CY} of 1

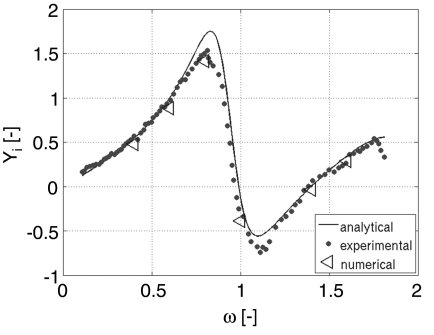

d) Imaginary part with apex angle Θ of 15 deg, Mach number of 0.08, and radii ratio of R_T/R_{CY} of 0.44

Fig. 4 Dimensionless admittance over dimensionless frequency.

planes, no additional eigenmode appears; that is, the dominating eigenfrequencies can be evaluated by means of the plots shown in Figs. 5c and 5d. Table 1 gives an overview of the resonance frequencies selected for later analysis. The first longitudinal mode, the three first transverse modes, and the first second transverse mode are chosen for the determination of the decay coefficient. In the case of Mach number scaling, the first longitudinal mode is hardly perceptible, which implies the mode is strongly damped.

The modes identified in the eigenmode analysis can be studied concerning their temporal evolution by means of a spectrogram. It offers the opportunity to analyze the amplitude of an eigenmode over time. The approach is based on a short-time Fourier transformation

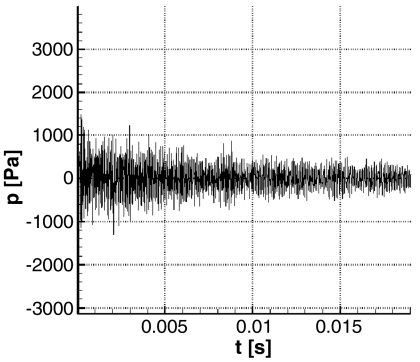

a) Timeline photoscaled

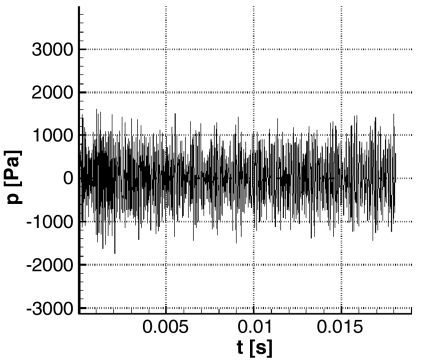

b) Timeline Mach-scaled

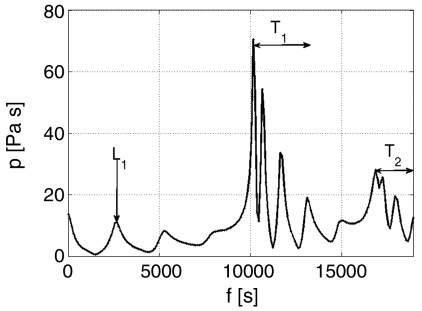

c) Eigenfrequency photoscaled design

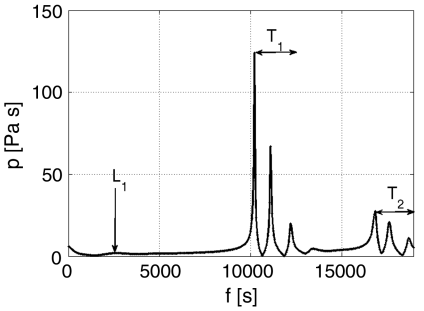

d) Eigenfrequency Mach-scaled design

Fig. 5 Pressure records and eigenfrequencies.

Table 1 Resonance frequencies of different designs

Photoscaled, Hz	Mach scaled, Hz	Mode class
2,620	2,540	Longitudinal
10,240	10,204	First transverse
10,640	11,080	First transverse
11,630	12,202	First transverse
16,850	16,817	Second transverse

Table 2 Decay coefficient for different designs

Photoscaled		Mach scaled	
f, Hz	α, s^{-1}	f, Hz	α, s^{-1}
2,620	1,459	2,540	2,887
10,240	11	10,204	−34
10,640	151	11,080	17
11,630	374	12,202	206
16,850	45	16,817	−9

using a special window. The results presented next are achieved with a hamming window. A tradeoff between time and frequency resolutions has to be found, which is controlled by the window length. At the eigenfrequencies, the lines of constant frequency can be extracted and approximated by an exponential fit. The α of the best-fitting exponential function is the decay coefficient of the eigenfrequency:

$$\left\{\partial \int_{t_b}^{t_e} [|\hat{p}(t)| - Ae^{-\alpha t}]^2\right\}/\partial\alpha = 0 \tag{2}$$

The higher the value of α, the better the damping and the less prone the design to combustion instabilities at this frequency. Figure 6 gives the decay coefficients for the photoscaled and Mach-scaled demonstrators evaluated at the eigenfrequencies shown previously. The longitudinal mode for the two designs can be found around 2600 Hz. It is apparent that the mode is heavily damped in the case of the Mach-scaled design. This was already indicated in the plots of the eigenfrequencies Fig. 5d. The next three eigenmodes for each design in the region between 10,000 and 13,000 Hz correspond to the eigenmodes with a first transverse contribution. Here, the results show the opposite behavior. The Mach-scaled thrust chamber is less stable than the photoscaled. The same can be found for the second transverse modes around 16,500 Hz. Furthermore, a general trend can be observed. T_1 modes with higher eigenfrequencies are damped stronger. The reason for this is that T_1 modes with higher eigenfrequencies are combined modes of longitudinal and transverse character. The higher the eigenfrequency, the higher the order of the longitudinal character. Hence, the angle between the wave front and the axial axis becomes smaller with increasing order of the longitudinal character of the transverse mode. Analyzing Fig. 6, it seems a smaller angle between the acoustic wave and the axial axis causes more damping; that is, the more the wave travels in the direction of the nozzle, the more it is damped. The results are also given in Table 2. The left side shows the results for the photoscaled thrust chamber, and the right side shows the results for the Mach-scaled thrust chamber. Note the decay coefficient for the first T_1 mode and the first T_2 mode is negative for the Mach-scaled design. This implies, together with Eq. (2), the amplitude of those modes increase over time. In fact, the time record of the pressure oscillations of the Mach-scaled design 5b shows almost no decaying. However, it does not show increasing oscillations either. This suggests acoustic oscillations of the first T_1 mode and the first T_2 mode are barely damped. It seems those two modes are fed by the other decaying modes. At this point, it cannot be said if this mode-coupling process is of physical or numerical nature. However, it can be assumed the damping of the two modes is very little but still damping. It would be desirable to see if the amplitude of the first T_1 mode and the first T_2 mode still grow at the time all other modes have been vanished. However, investigating this causes a great computational effort and has not yet been tackled. From the physical and computational background, it cannot be expected that an initial excitation causes growing amplitudes in the absence of any driving mechanism. Because the damping of the first T_1 mode and the first T_2 mode is very small in the photoscaled and Mach-scaled designs, neglecting other forms of damping (as proposed in [2]) constitutes an improper assumption. Buffum et al. [2] estimated the decay coefficient for viscous damping in cold flows with 5 s^{-1}, which is in the same range as the decay coefficient of the nozzle for pure transverse modes. Thus, for pure transverse modes, other forms of damping are at least equally important. Furthermore, a note on the numerical damping must be made. In general, the decay coefficient is influenced by all kinds of damping. Thus, numerical damping also has a contribution. A grid resolution study was carried out to minimize the influence of the numerical damping. The results of this study are depicted in Figs. 7a and 7b for the photoscaled and Mach-scaled designs, respectively. On the x axis of the plot, the refinement factor of the grid is given on the y-axis decay coefficient. The decay coefficient reaches a limit for the longitudinal mode and the first transverse modes concerning the grid resolution. However, the second transverse mode still shows a negative gradient, which implies grid convergence is not reached. Hence, only the decay coefficient for the longitudinal mode and the first transverse modes are verified.

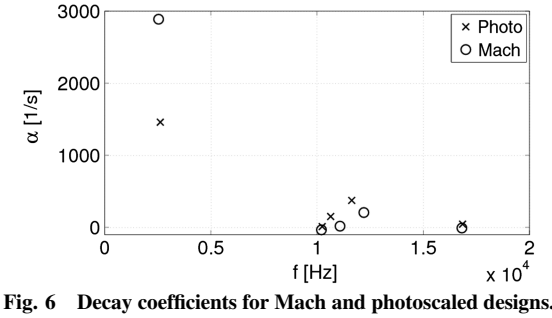

Fig. 6 Decay coefficients for Mach and photoscaled designs.

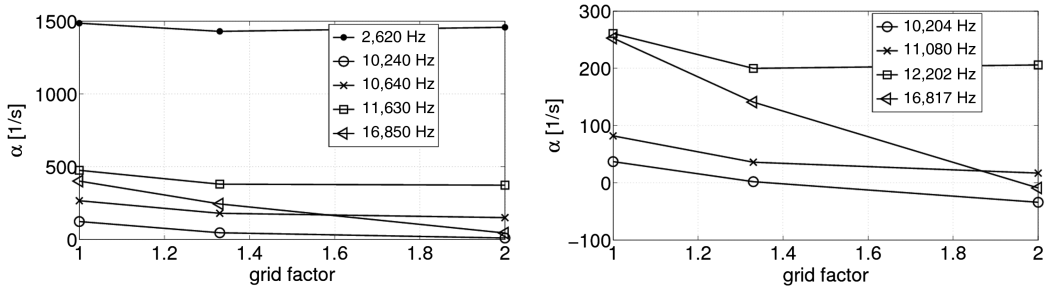

a) Photoscaled **b) Mach-scaled**

Fig. 7 Decay coefficients depending on grid resolution.

Table 3 Admittances for different designs

Photoscaled			Mach scaled		
f, Hz	Re(Y)	Im(Y)	f, Hz	Re(Y)	Im(Y)
2,620	−0.045	0.5869	2,540	1.2846	−0.8277
10,240	−0.1776	−0.1699	10,204	−0.2073	−0.127
10,640	−0.1628	−0.0709	11,080	−0.2381	0.8124
11,630	−0.1214	0.2237	12,202	−0.1408	0.085
16,850	−0.1816	−0.1887	16,817	−0.1937	−0.1187

VI. Nozzle Admittance

Another way to characterize the nozzle's impact on stability is to evaluate its admittance. It provides information on how much acoustic energy is lost by acoustic propagation through the nozzle. Furthermore, the admittance is often used in the framework of stability analyses, incorporating the entire propulsion system (e.g., by means of network models) to describe the influence of the nozzle. The admittance is defined as the ratio of the complex normal velocity and the complex pressure:

$$Y = \bar{\rho}\,\bar{c}\,\frac{\underline{n}\cdot\hat{u}}{\hat{p}} \tag{3}$$

The real part of the admittance indicates how much acoustic energy is lost through the nozzle by pure acoustic propagation. The bigger the real part, the more acoustic energy is propagated through the nozzle. The following relation can be given between admittance and pure acoustic energy transport:

$$\langle \underline{n}\cdot\underline{I}\rangle = \frac{1}{2}\frac{|\hat{p}|^2}{\bar{\rho}\,\bar{c}}\mathrm{Re}(Y) \tag{4}$$

where $\langle \underline{n}\cdot\underline{I}\rangle$ denotes the time-averaged acoustic flux normal to a surface, which only depends on the amplitude of the complex pressure and the real part of the admittance. Equation (4) reveals that the greater the real part of the admittance, the more energy is lost. For the investigation in this section, the admittance is determined directly at the entrance of the nozzle: i.e., at the third plane counting from the injector plane in the case of the photoscaled design and at the second plane from the injector plane for the Mach-scaled design. Special attention has to be paid to the axial position, where the admittance is evaluated. Presuming the shape of the mode is prescribed by analytical functions in circumferential (sine and cosine) and radial directions (Bessel function), the admittance is a function of the axial position only [4]. To compare the influence of the nozzle shape on damping, it is desirable to compare the two designs regarding their admittance at the end of the cylindrical part.

The procedure of evaluating the admittance is similar to the procedure obtaining the decay coefficient. The Gaussian pulse oscillates with a specific eigenfrequency. When the limit cycle is reached, the complex amplitude of pressure and velocity oscillations are evaluated and the ratio between both is calculated. The same is done for every eigenfrequency. Table 3 and Figs. 8a and 8b show the results of the real and imaginary parts of the two subscale demonstrators. Analyzing Fig. 8a, the real part of the admittance shows a similar trend as the decay coefficient. The longitudinal modes around 2600 Hz show a greater admittance than the rest. Especially for the Mach-scaled design, the admittance is very high, which implies much acoustic energy is propagated through the nozzle by the first longitudinal mode, even though it is not as clear as for the decay coefficient. The modes with a first transverse contribution in the region between 10,000 and 13,000 Hz show that the photoscaled design is more damped than the Mach-scaled one. In the case of the modes with second transverse contribution (frequency around 16,500 Hz), the admittances for photoscaled and Mach-scaled designs lie close together.

It is important to note that both cases, the photoscaled and Mach-scaled demonstrators, have negative real parts for all transverse modes. This implies that acoustic energy is propagating backward from the nozzle to the combustion chamber. Crocco and Sirignano [16] and Culick [17] describe this as the destabilizing character of the nozzle. Acoustic energy is transported back into the combustion chamber by pure wave transport. This argument is only true if pure acoustic transport is considered. In a moving fluid, additional terms for the transport of acoustic energy occur, which account for the convective transport. The sum of all those terms causes a time-averaged positive flux of acoustic energy, meaning acoustic energy is lost. The next section will show the relation between the different terms of the acoustic energy flux.

VII. Acoustic Energy Flux

Irrespective of the type of mean flow, a general conservation law for the energy of the perturbation quantities can be given [18]:

$$\frac{\partial E'}{\partial t} + \underline{\nabla}\cdot\underline{I}' = S' \tag{5}$$

Therefore, E' denotes the energy of the fluctuating quantities, I' denotes the flux of the fluctuating quantities, and S' denotes the source term. Depending on the complexity of the mean flow, more or less terms have to be considered for E', I', and S'. In the simplest case, where there is no mean flow, E' and I' equal the acoustic energy E_a and the acoustic flux I_a, respectively:

$$E_a = \frac{p'^2}{2\bar{c}^2\bar{\rho}} + \frac{\bar{\rho}\underline{u}'^2}{2} \qquad \underline{I}_a = p'\underline{u}' \qquad S' = 0 \tag{6}$$

The acoustic flux I_a can be converted into the form of Eq. (4). For a homentropic potential flow, E' and I' can still be substituted by the acoustic energy and the acoustic flux, respectively, but some additional terms are present in their definition:

$$E_a = \frac{p'^2}{2\bar{c}^2\bar{\rho}} + \frac{\bar{\rho}\underline{u}'^2}{2} + \frac{(\bar{u}\cdot\underline{u}')p'}{\bar{c}^2}$$

$$\underline{I}_a = p'\underline{u}' + \frac{p'^2\bar{u}}{\bar{\rho}\bar{c}^2} + \bar{\rho}(\bar{u}\cdot\underline{u}')\underline{u}' + \frac{p'}{\bar{c}^2}(\bar{u}\cdot\underline{u}')\bar{u} \qquad S' = 0 \tag{7}$$

Those terms also account for the convective transport. The source term is still zero. The preceding formulation can be applied in the

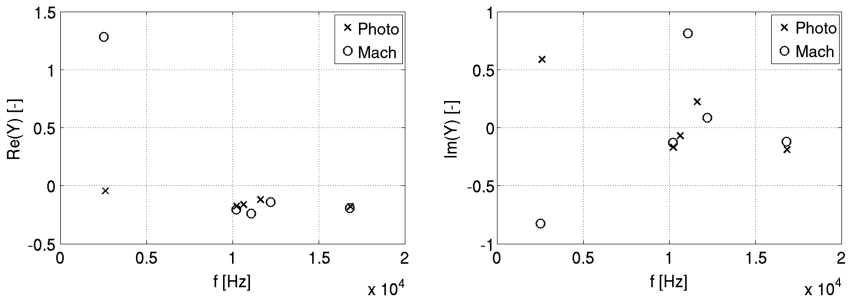

a) Real part **b) Imaginary part**

Fig. 8 Admittances.

analysis here. The flowfield in the thrust chamber, like that used in the current analysis, is homentropic and can indeed be treated as potential flow, as was shown by Candel [19]. If numerical damping is neglected, the only loss of acoustic energy occurs through the nozzle. Hence, integrating $\langle \underline{n} \cdot \underline{I}_a \rangle$ over a circular plane perpendicular to the axial axis provides the complete loss of acoustic energy. The acoustic flux averaged over one period can be written in the following form:

$$\underbrace{\langle \underline{n} \cdot \underline{I}_a \rangle}_{\text{flux}} = \frac{1}{T} \int_t^{t+T} \underline{n} \cdot \left[\underbrace{p' \underline{u}'}_{\text{term 1}} + \underbrace{\frac{p'^2 \bar{u}}{\bar{\rho} \bar{c}^2}}_{\text{term 2}} + \underbrace{\bar{\rho} (\bar{u} \cdot \underline{u}') \underline{u}'}_{\text{term 3}} + \underbrace{\frac{p'}{\bar{c}^2} (\bar{u} \cdot \underline{u}') \bar{u})}_{\text{term 4}} \right] \mathrm{d}\tau \tag{8}$$

where terms 1–4 denote the different contributions to the overall flux. By means of the admittance, Eq. (8) can be reformulated:

$$\underbrace{\langle \underline{n} \cdot \underline{I}_a \rangle}_{\text{flux}} = \frac{1}{2} \frac{|\hat{p}|^2}{\bar{\rho}\, \bar{c}} \left[\underbrace{\mathrm{Re}(Y)}_{\text{term 1}} + \underbrace{M}_{\text{term 2}} + \underbrace{M|Y|^2}_{\text{term 3}} + \underbrace{M^2 \mathrm{Re}(Y)}_{\text{term 4}} \right] \tag{9}$$

It becomes apparent that terms 1 and 4 are linearly dependent on $\mathrm{Re}(Y)$, term 3 depends on the square of the admittance, and term 2 is independent of the admittance. Term 2 only depends on the Mach number M. In the following, the contributions of the different terms to the overall flux are evaluated. The procedure is similar to the one explained for evaluating the admittance. The different eigenmodes will be excited by a Gaussian pulse oscillating with the eigenfrequency of the specific eigenmode. After a few cycles, the source is switched off. The pressure oscillations start decaying, and the different terms of eight are integrated over a window of the length of one cycle. The window is moved in time so that $\langle \underline{n} \cdot \underline{I}_a \rangle(t)$ is also a function of time. To be able to compare the results of the modes between designs, the different terms of nine are divided by the complete amount of acoustic energy transported through the nozzle since the source had been switched off:

$$\mathcal{E} = \int_{t_0}^{\infty} \int_{A_{\mathrm{cyl}}} \underline{n} \cdot \underline{I}_a(\tau)\, \mathrm{d}A\, \mathrm{d}\tau \qquad P = \left\langle \int_{A_{\mathrm{cyl}}} \underline{n} \cdot \underline{I}_a(t)\, \mathrm{d}A \right\rangle / E \tag{10}$$

The procedure is necessary, because at the time the source had been switched off, different amounts of acoustic energy are contained in the systems. Thus, the unit of the acoustic power P becomes $1/\mathrm{s}$. The results were taken at the third plane counting from the injector for the Mach-scaled and photoscaled demonstrators.

Figure 9a shows the contributions of the different terms in Eq. (8). The first longitudinal mode is excited at a frequency of 2620 Hz in the photoscaled design. There are three major contributions to the overall acoustic flux, which stem from terms 1–3. Term 4 plays only a minor role. Term 2 gives the biggest contribution to the overall flux. This term is not dependent on the admittance. In Fig. 9b, the contributions to the acoustic energy flux for the Mach-scaled design are shown. The excitation frequency is 2540 Hz. It shows that the decay of the overall flux is very strong. Here, term 3 has the biggest impact, but terms 1 and 2 are still in the order of magnitude. Figure 9c compares the two overall acoustic energy fluxes. It shows the Mach-scaled design rapidly looses acoustic energy compared with the photoscaled one. The Mach-scaled design starts with a bigger value and quickly drops below the curve of the photoscaled design. These results agree with what was found in the analysis of the decay coefficient (compare to Table 2). The longitudinal mode is damped very strongly in the Mach-scaled demonstrator.

Comparing the different terms of a first transverse mode of the photoscaled demonstrator, the importance of term 2 is emphasized. The excitation frequency lies at 11,630 Hz. The only terms that are of greater importance are terms 1 and 2, whereas term 2 is positive and term 1 is negative. This means term 1 causes acoustic energy to travel from the nozzle into the combustion chamber. However, it can also be seen that the convective transport is compensating the pure acoustic transport from term 1. The overall flux lies between term 1 and term 2 and is mainly directed outward. The same holds true for the Mach-scaled geometry. The excitation frequency is at 12,202 Hz. Term 1 and term 2 are strictly opposing each other, so the resulting energy flux is very small but still leaving the system. Comparing the flux of

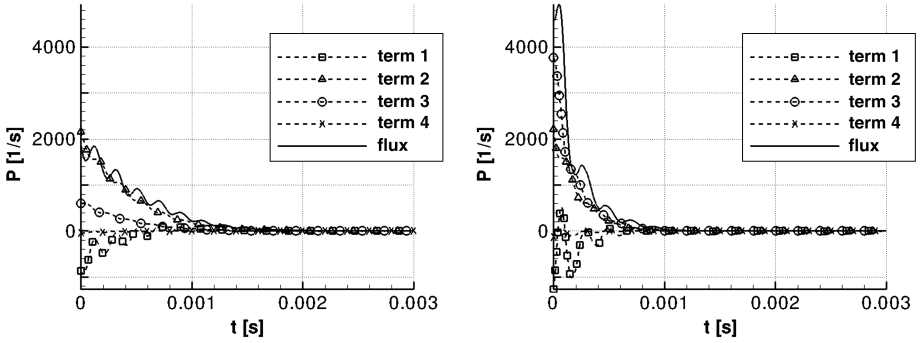

a) Photoscaled demonstrator excitation frequency 2620 Hz

b) Mach-scaled demonstrator excitation frequency 2540 Hz

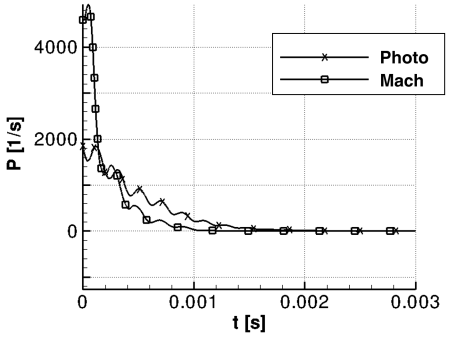

c) Comparison of the overall flux between Mach-scaled and photoscaled designs

Fig. 9 Acoustic fluxes over time for L_1 mode.

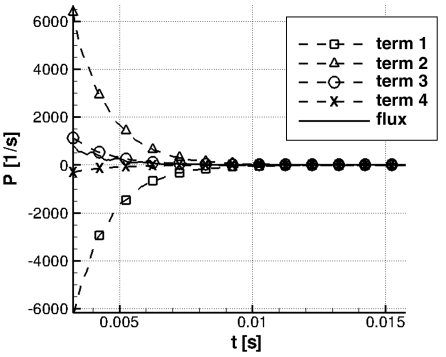

a) Photoscaled demonstrator excitation frequency 11,630 Hz

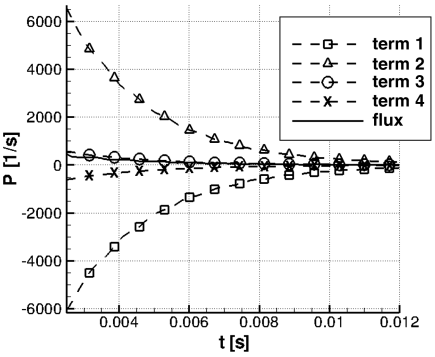

b) Mach-scaled demonstrator excitation frequency 12,202 Hz

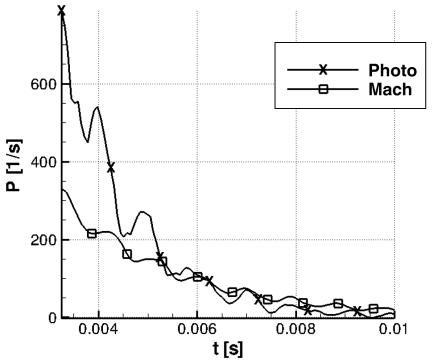

c) Comparison of the overall flux between Mach-scaled and photoscaled designs

Fig. 10 Acoustic fluxes over time for T_1 mode.

the overall energy of both geometries, it is apparent that the photoscaled design is more damped than the Mach-scaled design for the first transverse mode picked previously (see Fig. 10c). This is in accordance with what was found for the decay coefficient (see Table 2).

VIII. Conclusions

It was shown that PIANO-SAT is capable of investigating acoustic oscillations in a rocket engine. The influence of nozzle design on acoustic damping was shown for two different subscale demonstrators. Different characteristic quantities were presented, which were used under different conditions. The admittance can be used in network tools as a boundary condition at the end of the cylindrical part. Typically, network tools are applied to study combustion instability of the complete rocket engine, also incorporating fuel supply, combustion, etc. A negative value of the real part of the admittance is often interpreted as destabilizing the effect of the nozzle. Obviously, this may lead to the wrong conclusion: that acoustic energy is brought into the combustion chamber by the nozzle. Consulting the equations of the overall acoustic energy, it becomes clear, that acoustic energy is lost through the nozzle, even if the admittance is negative. The acoustic fluxes show the relation between the different contributions and illustrate the transport of acoustic energy through the nozzle. It was shown that the pure convective term played an important role and is independent of the admittance. Furthermore, the decay coefficient was measured. It accounts for the overall damping, independent of the physical mechanism of acoustic damping. It was found that the first longitudinal mode is heavily damped in the case of the Mach-scaled design, which makes the use of the Mach-scaled design as a subscale demonstrator preferable. However, the results change for the transverse modes. There, the Mach-scaled design behaves less stable compared with the photoscaled design. It is barely damped at all. If only longitudinal modes are considered, the choice for the demonstrator would be quite easy to make. However, as transverse modes could also be excited during combustion, one has to be careful here. For transverse modes, other forms of loss of acoustic energy are more important and control the damping of the oscillations. However, those are hardly assessable. At the moment, only the geometry of the thrust chamber is available. Hence, only the geometry can be evaluated. From the results of the preceding study, it appears reasonable to prefer the photoscaled design as a demonstrator. Even though the damping for the longitudinal mode is smaller, its stability concerning transverse modes is better; that is, a discernible amount of energy is lost through the nozzle. Later on, when the injector head is designed, more sophisticated stability analysis has to be carried out that also incorporates internal losses of oscillation energy in the combustor.

Acknowledgments

Financial support has been provided by the German Research Council (DFG) in the framework of the Sonderforschungsbereich Transregio 40. We would like to thank Astrium, GmbH, for providing us data and counsel for this work. The Leipniz–Rechenzentrum is gratefully acknowledged for providing computational resources. Additional thanks go to the DLR, German Aerospace Center, Braunschweig, for granting us access to the acoustic solver PIANO.

References

[1] Crocco, L., and Cheng, S., *Theory of Combustion Instability in Liquid Propellant Rocket Motors*, Butterworths Scientific, London, 1956.

[2] Buffum, F. G., Dehority, G. L., Slates, R. O., and Price, E. W., "Acoustic Attenuation Experiments on Subscale, Cold-Flow Rocket Motors," *AIAA Journal*, Vol. 5, No. 2, 1967, pp. 272–280. doi:10.2514/3.3952

[3] Marble, F. E., and Candel, S. M., "Acoustic Disturbance Form Gas Non-Uniformities Convected Through a Nozzle," *Journal of Sound and Vibration*, Vol. 55, No. 2, 1977, pp. 225–243. doi:10.1016/0022-460X(77)90596-X

[4] Bell, W. A., "Experimental Determination of Three-Dimensional Liquid Rocket Nozzle Admittances," Ph.D. Thesis, Georgia Inst. of

Technology, Atlanta, 1972.
[5] Zinn, B. T., "Review of Nozzle Damping in Solid Rocket Instabilities," AIAA/SAE 8th Joint Propulsion Specialist Conference, New Orleans, LA, AIAA Paper 1972-1050, 1972.
[6] Bell, W. A., and Zinn, B. T., "The Prediction of Three-Dimensional Liquid Rocket Nozzle Admittances," NASA CT-121129, 1973.
[7] Cantrell, R. H., and Hart, R. W., "Interaction Between Sound and Flow in Acoustic Cavities: Mass, Momentum and Energy Considerations," *Journal of the Acoustical Society of America*, Vol. 36, No. 4, 1964, pp. 697–706. doi:10.1121/1.1919047
[8] Morfey, C. L., "Acoustic Energy in Non-Uniform Flows," *Journal of Sound and Vibration*, Vol. 14, No. 2, 1971, pp. 159–170. doi:10.1016/0022-460X(71)90381-6
[9] Pieringer, J. E., "Simulation Selbserregter Verbrennungsschwingungen in Raketenschubkammern," Ph.D. Thesis, Technical Univ. of Munich, Munich, 2008.
[10] Pieringer, J. E., Fassl, F., and Sattelmayer, T., "Simulation of Combustion Instabilities in Liquid Rocket Engines with Acoustic Perturbation Equations," *Journal of Propulsion and Power*, Vol. 25, No. 5, 2009, pp. 1020–1031. doi:10.2514/1.38782
[11] Delfs, J. W., Grogger, H. A., and Lauke, T. G. W., "Numerical Simulation of Aeroacoustic Noise by DLR's Aeroacoustic Code PIANO," DLR, German Aerospace Center, Braunschweig, 2002.
[12] Ianniello, S., Delfs, J., and Lauke, T., "CAA Simulation of Sound Generation by Linear Interaction of Vorticity with a Wedge," *Journal of Sound and Vibration*, Vol. 249, No. 2, 2002, pp. 351–353. doi:10.1006/jsvi.2001.3845
[13] Ewert, R., Dierke, J., Appel, C., and Herr, M., "RANS/CAA Based Prediction of NACA 0012 Broadband Trailing Edge Noise and Experimental Validation," 15th AIAA/CEAS Aeroacoustics Conference, Miami, FL, AIAA Paper 2009-3269, 2009.
[14] Pieringer, J. E., and Sattelmayer, T., "Simulation of Thermo-Acoustic Instabilities Including Mean Flow Effects in the Time Domain," *Proceedings of the Thirteenth International Congress on Sound and Vibration (ICSV13)* [CD-ROM], Vienna, edited by J. Eberhardsteiner, H. A. Mang, and H. Waubke, Vienna Univ. of Technology, Vienna, 2006.
[15] Ewert, R., and Schröder, W., "Acoustic Perturbation Equations Based on Flow Decomposition via Source Filtering," *Journal of Computational Physics*, Vol. 188, No. 2, 2003, pp. 365–398. doi:10.1016/S0021-9991(03)00168-2
[16] Crocco, L., and Sirignano, W. A., "Behavior of Supercritical Nozzles Under Three-Dimensional Oscillatory Conditions," AGARDograph 117, 1967.
[17] Culick, F. E. C., "Combustion Instabilities in Liquid-Fueled Propulsion Systems an Overview," *Combustion Instabilities in Liquid Fueled Propulsion Systems*, AGARD, CP 450, Nos. 1–2, 1988, pp. 1–73.
[18] Myers, M. K., "Transport of Energy by Disturbances in Arbitrary Steady Flows," *Journal of Fluid Mechanics*, Vol. 226, 1991, pp. 383–400. doi:10.1017/S0022112091002434
[19] Candel, S. M., "Acoustic Conservation Principles and an Application to Plane and Modal Propagation in Nozzles and Diffusers," *Journal of Sound and Vibration*, Vol. 41, No. 2, 1975, pp. 207–232. doi:10.1016/S0022-460X(75)80098-8

T. Lin
Associate Editor